Multiple Coulomb Scattering of Muons on Lithium Hydride

The MICE collaboration

Multiple Coulomb Scattering (MCS) is a well known electromagnetic phenomenon experienced by charged particles traversing absorbing materials. However, measurements of muons traversing low-Z materials by the MuScat experiment showed that different theoretical models and simulation codes, such as the Molière model and GEANT4 (v7.0), overestimate the scattering of muons in low-Z materials. The Muon Ionization Cooling Experiment (MICE) measures cooling of a muon beam traversing liquid hydrogen or lithium hydride (LiH) for the design of future accelerator facilities, such as a Neutrino Factory or a Muon Collider. The energy loss and MCS in the absorber are competing effects that affect the performance of the cooling channel. Therefore, measurements of MCS are required to validate the predicted muon ionization cooling performance at future accelerator facilities. In this paper, we report on the first measurement of MCS using a LiH absorber in the muon momentum range 160 MeV/c to 255 MeV/c. These measurements show agreement with the Molière model and with the GEANT4 (v9.6) simulation code as a function of incoming muon momentum.

1 Introduction

Multiple Coulomb Scattering (MCS) describes the multiple interactions of charged particles in the Coulomb field of the atoms of a material. Greisen and Rossi derived a simple expression for the root-mean-squared (RMS) scattering angle in the small angle approximation [1] by integrating the Rutherford cross section [2]. The variance of the scattering angle $\langle\theta^2\rangle$ after multiple collisions traversing a thickness Δz of material, could be simply expressed as a function of its radiation length X_0:

$$\frac{\langle\theta^2\rangle}{\Delta z} = \frac{E_s^2}{p^2\beta^2}\frac{1}{X_0}, \tag{1}$$

where $E_s = 21.2\,\text{MeV/c}$, p is the momentum of the charged particle and β its speed in units of the speed of light c. The projection of the scattering angle on a plane gives the RMS projected scattering angle $\theta_0 = \sqrt{\langle\theta^2\rangle}/2$, which is determined to be:

$$\theta_0 = \frac{14.85\ \text{MeV/c}}{p\beta}\sqrt{\frac{\Delta z}{X_0}}. \tag{2}$$

Molière [3, 4] developed a theory of MCS based on the scattering of electrons from the atomic nuclei and showed good agreement with data. Bethe [5] additionally took into account interactions with electrons in the atom, which was subsequently corrected by Fano [6] to account for elastic and inelastic cross-sections.

Most of these theories reproduce very well the MCS data for small angles and at large values of the atomic number Z. Highland [7] compared the Molière theory with the simple formula by Rossi (equation 1), and found that there was a distinct Z dependence on the value of E_s. As a consequence, Highland recommends to add a logarithmic term to the Rossi formula to improve the agreement with the Molière theory, especially at low values of Z. The formula for θ_0, the RMS width of the Gaussian approximation for the central 98% of the projected scattering angle distribution on a plane, was reviewed by Lynch and Dahl [8] and is now recommended by the Particle Data Group [9]:

$$\theta_0 = \frac{13.6\ \text{MeV/c}}{p\beta}\sqrt{\frac{\Delta z}{X_0}}\left(1 + 0.038\ln\frac{\Delta z}{X_0}\right), \tag{3}$$

being accurate to 11% in the full range of values of Z.

Multiple scattering has not been well modelled for low Z absorbers in standard simulations. Data collected by the MuScat experiment [10] indicates that GEANT4 (v7.0) [11] and the Molière model overestimate MCS for these materials. However, a simple Monte Carlo method, which samples the Wentzel scattering cross section to generate the MCS distributions [12] as separate interactions within a material, was shown by Carlisle and Cobb in [13] to agree very well with muon scattering data from the MuScat experiment.

The Muon Ionization Cooling Experiment (MICE) [14] made measurements of emittance reduction in low-Z absorbers, such as liquid hydrogen and lithium hydride, and has demonstrated ionization cooling for the first time [15]. This technique can be used to cool beams of muons for a Neutrino Factory [16] or a Muon Collider [17]. The emittance of the muon beam [18] is increased by the scattering in the absorber material and reduced due to energy loss. The change in the normalized emittance ϵ_n [19] is given by

$$\frac{d\epsilon_n}{dz} \approx -\frac{\epsilon_n}{p_\mu \beta}\left\langle \frac{dE_\mu}{dz} \right\rangle + \frac{\beta_\perp p_\mu}{2m_\mu}\frac{d\theta_0^2}{dz} \tag{4}$$

where $\frac{dE_\mu}{dz}$ is the energy loss of muons. The normalized emittance is $\epsilon_n = \sqrt[4]{det(Var(x,y,p_x,p_y))}/m_\mu$, where $det(Var(x,y,p_x,p_y))$ is the determinant of the covariance matrix for a beam, with a muon mass m_μ, a momentum p_μ, relativistic velocity $\beta = v_\mu/c$, and a transverse momentum distribution with a betatron function given by $\beta_\perp$.

For MICE to make accurate predictions of the emittance in the absorber materials, the model in the simulation must be validated. This is particularly important for the prediction of the equilibrium emittance, the case when $d\epsilon_n/dz = 0$ and

$$\epsilon_n = \frac{\beta_\perp p_\mu^2 \beta}{2m_\mu}\frac{d\theta_0^2}{dz}\left\langle \frac{dE_\mu}{dz} \right\rangle^{-1}. \tag{5}$$

This provides the minimum emittance for which cooling is effective.

Therefore, there is great interest in performing a detailed measurement of MCS from muons impinging on low-Z absorbers, such as liquid hydrogen or lithium hydride (LiH). In this paper, we perform the first measurement of MCS from muons on lithium hydride in the muon momentum range 160 MeV/c to 255 MeV/c using the MICE apparatus. These measurements are relevant for the design of the cooling channel for a Neutrino Factory or Muon Collider. This paper is divided as follows: Section 2 describes MICE, demonstrates the method and defines the relevant measurement angles, Section 3 describes the data collected and the event selection, Section 4 describes the data deconvolution method and the multiple scattering results, with a final short conclusion in Section 5.

2 Method

The Muon Ionization Cooling Experiment (MICE) configuration for the MCS measurements consisted of two scintillating fibre trackers upstream and downstream of a lithium hydride (LiH) absorber. Each tracker contained five scintillating fibre triplet planes immersed in helium gas arranged symmetrically about the absorber [20]. The tracker planes were labelled so that plane 5 was always the furthest from the absorber for both the upstream and downstream trackers. Aluminium vacuum windows separated the helium volume from the vacuum containing the absorber. The tracker position resolution was determined to be 661 μm. A solenoidal magnet surrounded the MICE trackers, but the magnetic field was turned off for these measurements to perform straight-track reconstruction of the muons before and after the absorber.

The muon beam was from 800 MeV protons at the ISIS synchrotron facility at the Rutherford Appleton Laboratory [18, 19] impinging on an insertable titanium target [21, 22] to extract pions into a beam line consisting

of two dipole magnets for pion and muon momentum selection, a decay solenoid to increase the decay volume for the pions, and nine quadrupole magnets for beam focusing and beam matching.

A time-of-flight (TOF) system, consisting of three detectors (TOF0 and TOF1 upstream and TOF2 downstream of the cooling channel), was used to extract the momentum for well-reconstructed muons [23]. Furthermore, a Cherenkov detector and pre-shower system (named KL) were used for particle identification [18, 24]. Finally, an Electron-Muon Ranger was used to independently measure the energy of a stopping muon in this calorimeter [25]. A schematic diagram of the MICE cooling channel and ancillary detectors is shown in Fig. 1. The MICE coordinate system has $+z$ pointing along the beam direction downstream, $+y$ points upwards and $+x$ is defined to have standard right-handed coordinates.

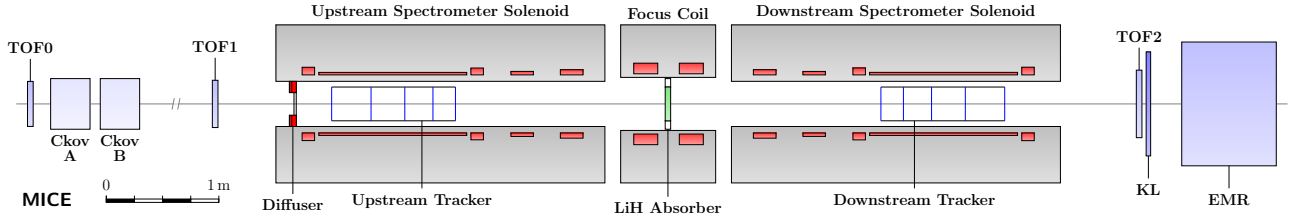

Figure 1: MICE cooling channel.

The MICE LiH absorber was a cylindrical disk, 65.0±0.25 mm in thickness (along the z-axis) and with a 55 cm diameter coated with a thin parylene layer. The LiH composition consisted of 81% ^{6}Li, 4% ^{7}Li, 14% ^{1}H with some trace amounts of carbon, oxygen and calcium. The density of the disk was measured to be 0.694±0.003 g/cm^3, and the radiation length was calculated to be 70.38 g/cm^2.

Multiple scattering is characterized using either the three-dimensional (3D) angle between the initial and final momentum vectors or the difference of angles that those vectors make when projected onto a given coordinate plane. The former is expressed mathematically as

$$\theta_{Scatt} = \text{acos}\left(\frac{\mathbf{p}_{US}\cdot\mathbf{p}_{DS}}{|\mathbf{p}_{US}||\mathbf{p}_{DS}|}\right) \tag{6}$$

where $\mathbf{p}_{US}$ and $\mathbf{p}_{DS}$ are the momentum vectors measured by the upstream and downstream trackers, respectively. Alternatively, the projection of the scattered track onto two perpendicular planes (the Y-Z and X-Z planes) that contain the incident track defines the projected scattering angles θ_x and θ_y, which are also used in the analysis. These are defined mathematically in the Appendix.

Table 1 shows the expected RMS scattering angle, θ_0, using Equation 3, for the LiH absorber and the material found in each of the trackers. The tracker material is significantly less than the absorber material.

3 Selected Data and Reconstruction

3.1 Data Collection

Six data sets were compiled during the ISIS user cycle 2015/14 using a muon beam with a nominal 3 mm emittance at three different nominal momenta (172 MeV/c, 200 MeV/c and 240 MeV/c), with and without the lithium hydride (LiH) absorber in place. The beams typically had RMS widths of $30-36$ mm and divergences of $9.0-9.4$ mrad. The empty absorber data is used to determine the scattering effect attributed to the tracking detectors and is used to extract the MCS distribution due to the absorber in a deconvolution method, described in Section 4. The positive muon beam was selected to ensure that it contained less than 1.4% pion contamination

Table 1: Material budget affecting tracks passing through the MICE LiH absorber. The material thickness normalized by the radiation length is given with the RMS of the scattering distribution calculated from the full PDG formula [9] in eq. 3. Note that the effective thickness shown for the tracker materials (He, Al windows and Scint. Fibres) is for one tracker.

				θ_0 (mrad)		
Material	z (cm)	z/X_0	ρ (g cm^{-3})	172 MeV/c	200 MeV/c	240 MeV/c
Tracker He	113	0.0002	1.663×10^{-4}	0.888	0.736	0.592
Al Window	0.016	0.0018	2.699	2.99	2.48	2.00
Scint. Fibres	0.74	0.0180	1.06	10.55	8.74	7.04
Total Tracker		0.020		11.17	9.26	7.45
LiH	6.5	0.0641	0.694	21.04	17.44	14.04
Total with LiH		0.0841		24.38	20.20	16.27

[24]. The positron contamination is identified through the time-of-flight system, with a time of flight between TOF0 and TOF1 of less than 26 ns, and is not included in the data sample. The trigger condition to accept events in the detector is to have a hit in the TOF1 counter.

3.2 Selection

The three nominal muon beams are merged into one sample, and all muons in the sample are treated identically. Unbiased scattering distributions were selected from the data samples using the cuts provided in Table 2. The fraction of events selected by each cut is also shown. Events that produce one space point in TOF0 and one space point in TOF1 are selected to ensure that the muon momenta are well measured. The diffuser, which is used to set the beam emittance, was fully retracted for all of the runs used to measure multiple scattering. However, there is a small probability for muons to traverse the diffuser ring in its retracted position, adding extra scattering material with respect to other selected tracks. A cut to remove any upstream tracks that traversed the outer ring of the MICE diffuser is implemented, since the momentum is not well measured for these tracks.

A fiducial selection to ensure that the downstream track is reconstructible in the downstream tracker is also applied. If the upstream track is projected to the downstream tracker plane 5 and the track falls outside of a fiducial radius of the detector ($r_0 = 90$ mm), then the track is rejected. Finally, a χ^2 per degree of freedom cut (χ^2/NDF < 4) is applied to remove badly reconstructed tracks, both upstream and downstream. Particles are selected with a time of flight between stations TOF0 and TOF1 (Δt_{01}) within a timing window compatible with the particle being a muon (above 26 ns), which rejects all positrons in the beam. The data is then binned in 200 ps TOF01 bins (Figure 2). Three samples were selected for more careful scrutiny. The samples corresponding to 172 MeV/c and 240 MeV/c momenta contain 0.19% of the events selected and, for the 200 MeV/c momentum, it contains 0.25% of the events.

3.3 Reconstruction

Data reconstruction and simulation were carried out using MAUS (3.3.2) [27], the MICE Analysis and User Software package. Upstream tracks are required to be reconstructed (with a minimum of three hits in the five upstream tracker planes), but no requirement is made on the downstream track being present. A downstream track that is not reconstructed or with a projected reconstruction outside the fiducial area of the last downstream tracker plane, is accounted in an overflow bin, to ensure that the normalisation is accurate. The efficiency of

Table 2: Simple particle selection criteria and survival rates for 172 MeV/c, 200 MeV/c and 240 MeV/c simulated muon samples with a LiH absorber.

Selection	Description	Fraction events surviving each cut
Upstream track selection	Exactly one TOF0 space point, exactly one TOF1 space point and one US track (if there is no DS track $\theta_x = \theta_y = 45°$).	100.0%
Diffuser cut	US tracks are projected to the diffuser position, any track within the radius of the diffuser annuli is rejected.	81.73%
Fiducial selection	For projected US tracks $\sqrt{x^2+y^2} < r_0$ at plane 5 of DS tracker, where $x = x_0 + (\frac{dx}{dz}\Delta z)$, $y = y_0 + (\frac{dy}{dz}\Delta z)$ and $r_0 = 90$ mm.	3.7%
χ^2 cut	χ^2/NDF < 4 upstream and downstream	3.7%
TOF timing selection	Select muons from run at the target momentum.	0.19%-0.25%

the trackers has been shown to be very close to 100% [28].

The reconstruction acceptance of the downstream tracker as a function of the projected scattering angles θ_x and θ_y is shown in Fig. 3. The acceptance depends strongly on the scattering angle so the scattering angle distributions compiled from the data after all selections must be corrected by the acceptance measured from simulation after the same selection. A sixth order symmetric polynomial fit to the efficiency,

$$\epsilon = a + b\theta_i^2 + c\theta_i^4 + d\theta_i^6,$$

where $i = x, y$ and a, b, c, d are fit parameters, is carried out to avoid fluctuations in the tails of the acceptance function.

The distance between the selected upstream and downstream tracks at the centre of the absorber is on average 36 mm, compatible with a track scattering in the LiH absorber. A residual misalignment between the upstream and downstream trackers is corrected by rotating all upstream tracks by a fixed angle in order to minimise the mean of the asymmetry distribution as a function of scattering angle in θ_x and θ_y. The final uncertainty in the rotation angles from the misalignment procedure is 0.07 mrad.

The time of flight is used to measure the momentum of the muon at the absorber, calculated as

$$p_\mu = \frac{m_\mu c}{\sqrt{\frac{t_\mu^2}{t_e^2} - 1}}, \tag{7}$$

where t_μ is the time of flight of the muon and and t_e is the average time of flight of positrons ($t_e = 25.40$ ns for TOF01 and 27.38 ns for TOF12). If the muon reaches the end of the channel, the measurement is made using TOF1 and TOF2. In the case that no hit is recorded in TOF2 then the momentum measurement is made using the upstream information from TOF0 and TOF1 (Fig. 4), applying a correction to account for the energy loss in the channel, using the Bethe-Bloch expression for the most probable energy loss [9]. Examples of time-of-flight window selections from TOF01 and their momentum measurement measured using TOF12 are shown in Table 3.

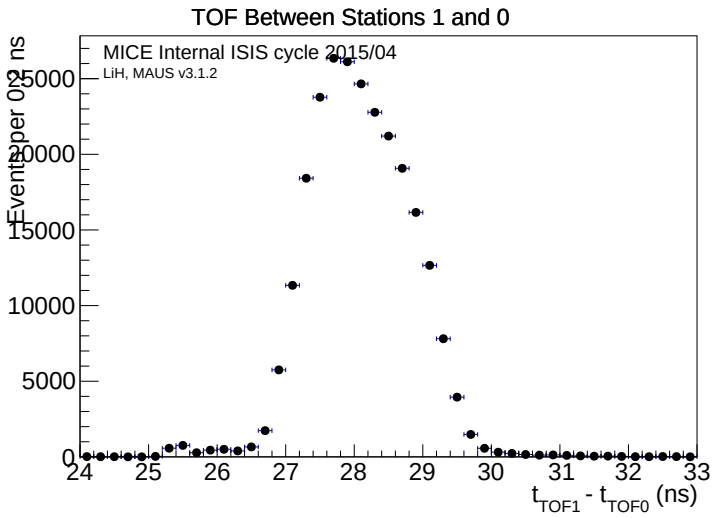

Figure 2: Combined TOF distribution of LiH absorber data for all beamline settings.

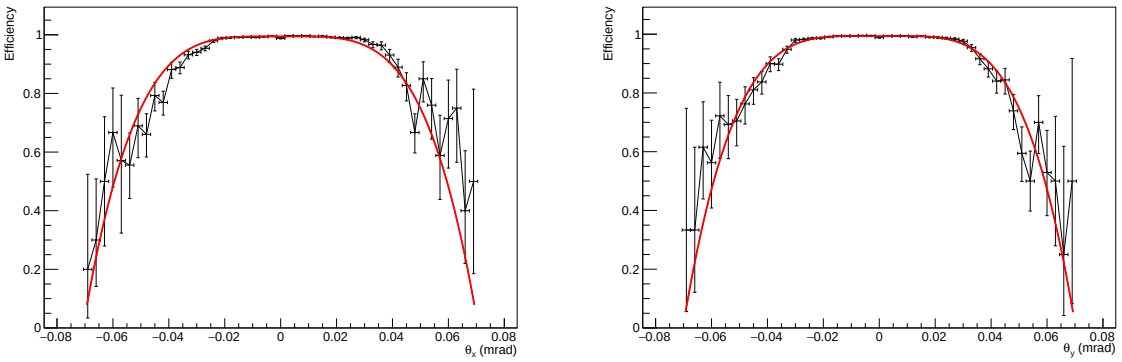

(a) Efficiency in θ_x.

(b) Efficiency in θ_y.

Figure 3: The fraction of events reconstructed by the trackers as a function scattering angle after event selection. The red line is a fit to a symmetric sixth order polynomial used for the efficiency correction.

Table 3: Time-of-flight selections between stations 0 and 1 corresponding to specific axial mean momenta and standard deviations measured by the time of flight between stations 1 and 2 (from Figure 6) and momentum resolution for each bin. This table will be re-done with the actual 172, 200 and 240 MeV/c bins.

Momentum (MeV/c)	Lower limit (ns)	Upper limit (ns)	Measured $\langle p \rangle$ (MeV/c)	Standard deviation (MeV/c)	Momentum Resolution (MeV/c)
172	28.64	28.84	170.48±0.09	6.17±0.06	4.62
200	27.95	28.15	196.96±0.09	8.09±0.07	5.75
240	27.25	27.45	234.56±0.15	11.68±0.11	7.91

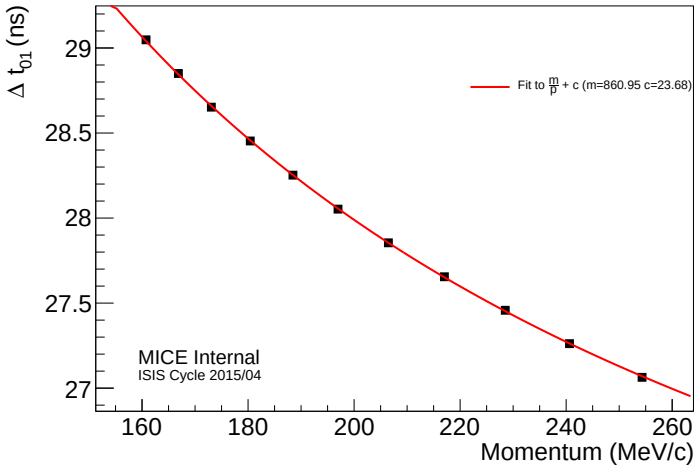

Figure 4: Time of flight between TOF0 and TOF1 (Δt_{01}) as a function of momentum for each 200 ps sample.

3.4 Comparison to simulation

The agreement between the calculated reconstructed momentum and the simulated true muon momentum at the centre of the absorber is shown in Fig. 5(a) and a residual plot is shown in Fig. 5(b). A comparison between the momentum distribution for the three different sample momenta (172 MeV/c, 200 MeV/c and 240 MeV/c) is shown in Fig. 6.

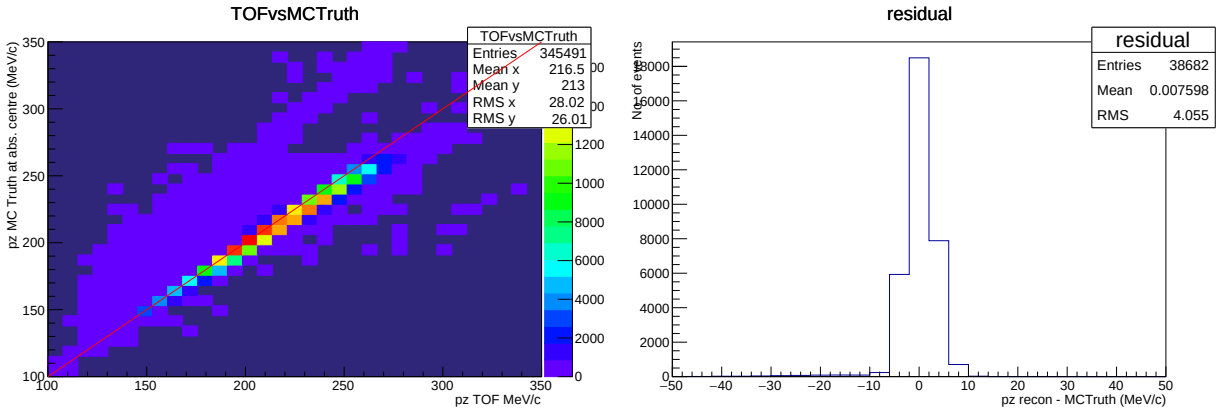

(a) Reconstructed momentum at centre of absorber from TOF calculation, compared to simulated momentum.

(b) Residuals between reconstructed momentum and true simulated momentum.

Figure 5: Time-of-flight and momentum distributions for the simulated muon beam with the LiH absorber.

A comparison between the x and y positions of selected muons upstream for the GEANT4 (v9.6) simulations and for data at 200 MeV/c is shown in Fig. 7, showing good agreement. The θ_x and θ_y distributions from the LiH and empty absorbers are compared to GEANT4 (v9.6) simulations in Figs. 8, 9, 10 at three different momenta 172 MeV/c, 200 MeV/c and 240 MeV/c. Good agreement with simulation is observed.

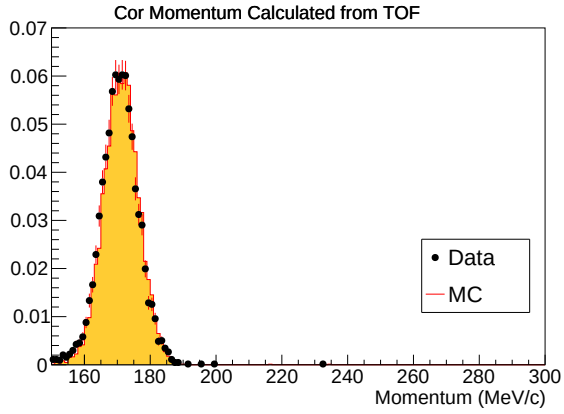

(a) Selected muons p_z distribution at the centre of the absorber for the 172 MeV/c sample.

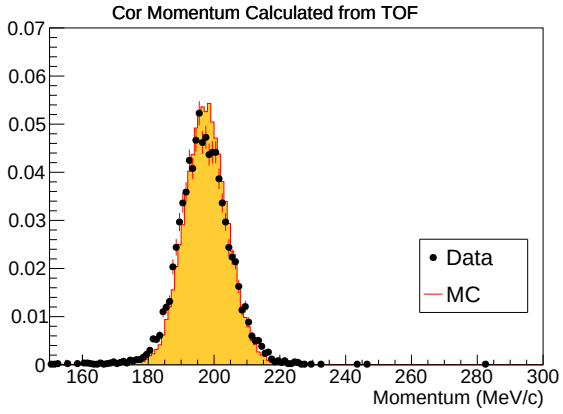

(b) Selected muons p_z distribution at the centre of the absorber for the 200 MeV/c sample.

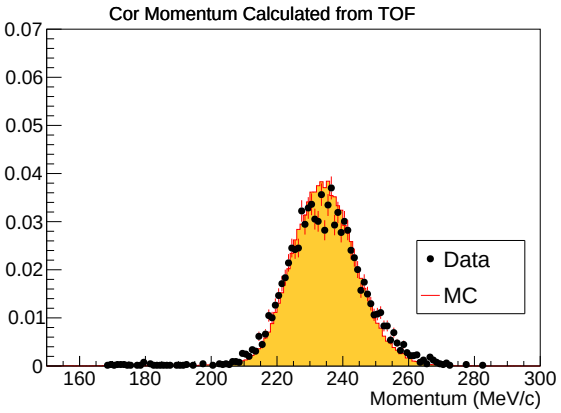

(c) Selected muons p_z distribution at the centre of the absorber for the 240 MeV/c sample.

Figure 6: Comparison of measured muon momentum between Monte Carlo simulation (MC) and data with the LiH absorber at different momenta.

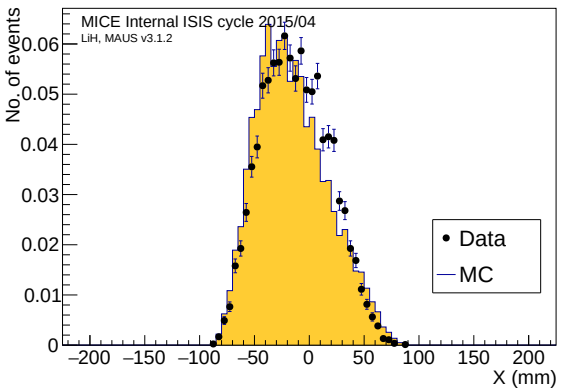

(a) Selected muons x distribution at upstream reference plane.

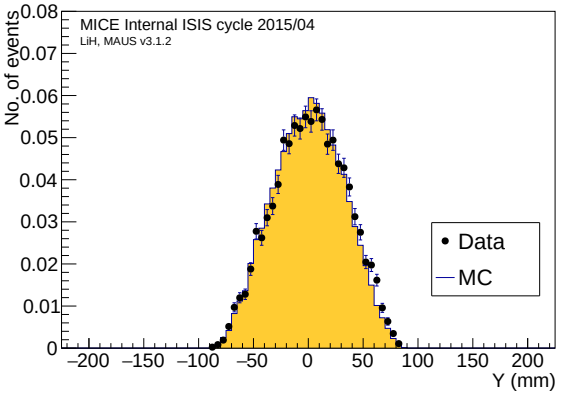

(b) Selected muons y distribution at upstream reference plane.

Figure 7: Comparison between GEANT4 (v9.6) Monte Carlo simulations (MC) and data for selected muons with the LiH absorber at 200 MeV/c.

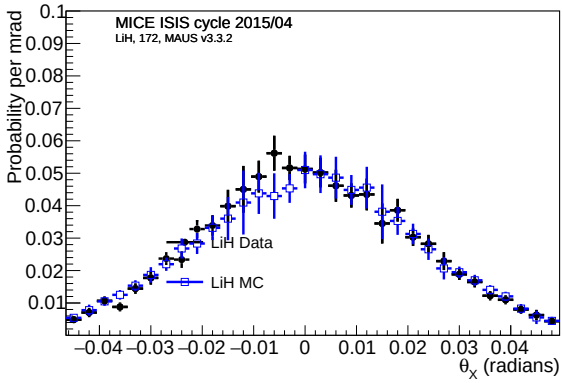

(a) θ_x scattering of μ^+in LiH.

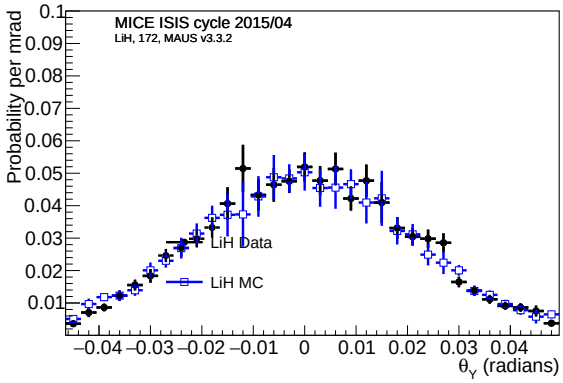

(b) θ_y scattering of μ^+in LiH.

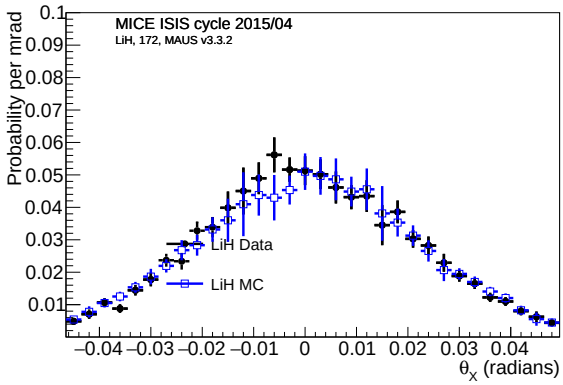

(c) θ_x scattering of μ^+in empty absorber.

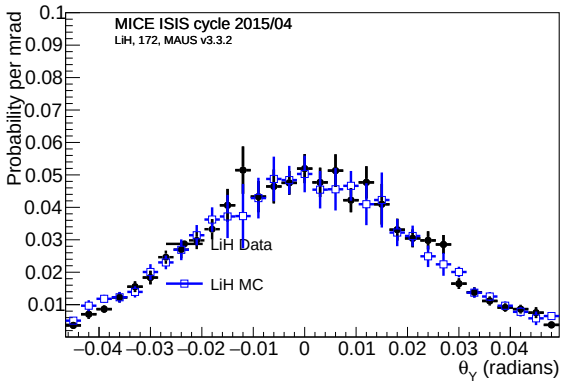

(d) θ_y scattering of μ^+in empty absorber.

Figure 8: Scattering distributions θ_x and θ_y reconstructed from the 172 MeV/c muon beam with the LiH absorber in place (top) and for the empty absorber (bottom) (the plots are place-holders for the time being) compared to MC scattering distributons.

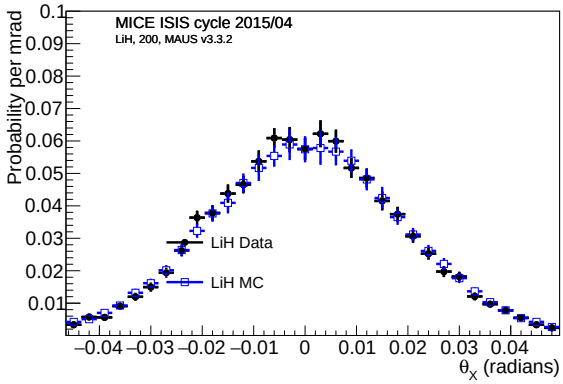

(a) θ_x scattering of μ^+in LiH.

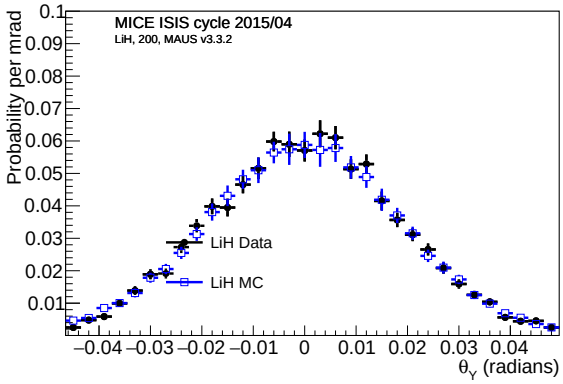

(b) θ_y scattering of μ^+in LiH.

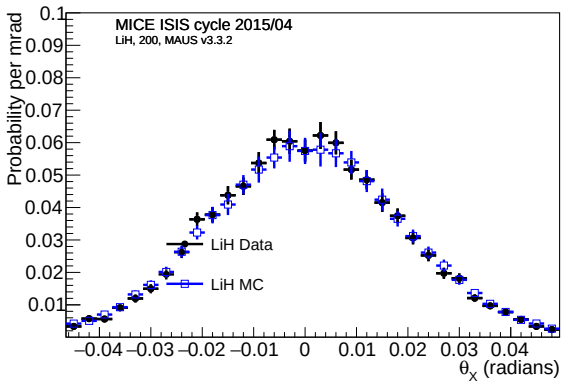

(c) θ_x scattering of μ^+in empty absorber.

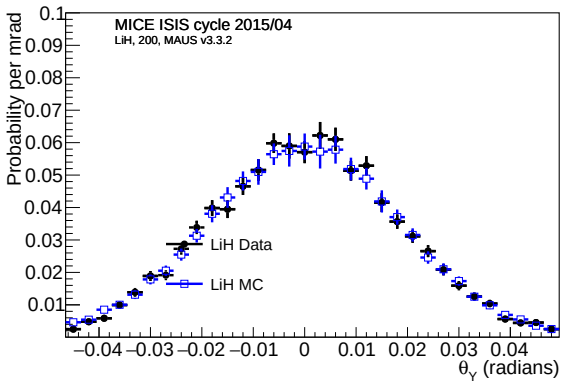

(d) θ_y scattering of μ^+in empty absorber.

Figure 9: Scattering distributions reconstructed from the 200 MeV/c muon beam with the LiH absorber in place (top) and for the empty absorber (bottom) (the plots are place-holders for the time being) compared to MC scattering distributons.

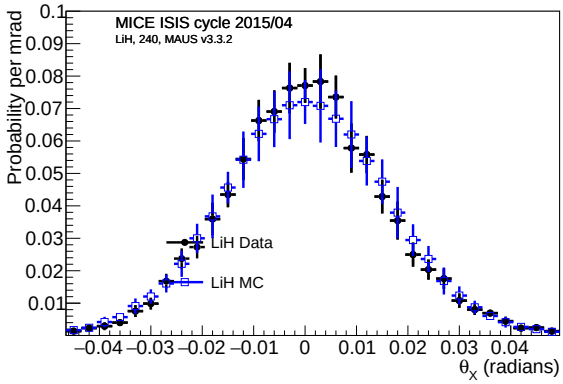

(a) θ_x scattering of μ^+in LiH.

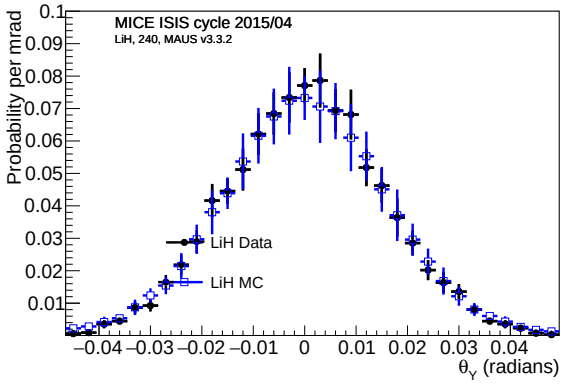

(b) θ_y scattering of μ^+in LiH.

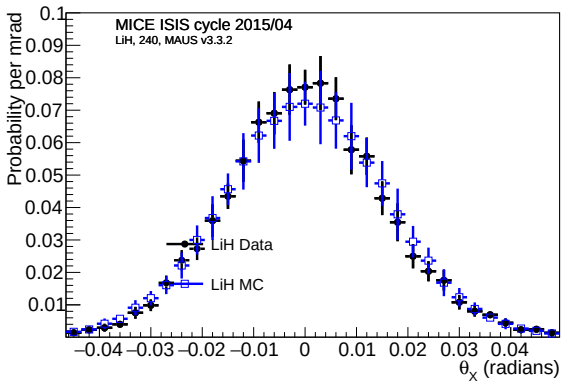

(c) θ_x scattering of μ^+in empty absorber.

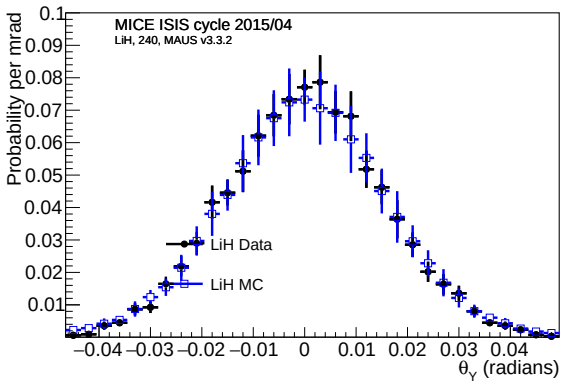

(d) θ_y scattering of μ^+in empty absorber.

Figure 10: Scattering distributions reconstructed from the 240 MeV/c muon beam with the LiH absorber in place (top) and for the empty absorber (bottom) (the plots are place-holders for the time being) compared to MC scattering distributons.

4 Data Deconvolution and Results

4.1 Convolution with Scattering Models

The data collected with the absorber is compared with the MCS models by performing a convolution of the scattering model with zero-absorber data. The convolution is achieved by adding an angle sampled from the predicted scattering distribution in the absorber for a given model (GEANT4 or Molière) to the angles determined from a given trajectory selected from the zero-absorber (empty channel) data, to take into account the scattering from the measurement system. The trajectories described by the sum of angles are extrapolated to the downstream tracker and those trajectories that do not appear in the downstream tracker are then treated as overflow events. The net effect is a distribution $n_{conv.}(\theta)$ that is the convolution of the raw scattering model $n_{model}(\theta)$ with the detector effects given by the zero-absorber distribution $n_{zero}(\theta)$ within the acceptance.

The residuals between the scattering with the LiH absorber in data $n_{data}(\theta_i^{rec})$ and those predicted by the models $n_{conv.}(\theta_i^{rec})$ using

$$\chi^2 = \sum_{i=0}^{N} \frac{(n_{data}(\theta_i^{rec}) - n_{conv.}(\theta_i^{rec}))^2}{n_{data}(\theta_i^{rec}) + n_{conv.}(\theta_i^{rec}) + \sum \sigma_{sys,i}^2} \tag{8}$$

contained in the ith reconstructed angle bin θ_i^{rec} are calculated in an iterative manner until these converge. The systematic uncertainties $\sigma_{sys,i}^2$, discussed in Sub-section 4.3, are calculated and summed on a bin by bin level. Plots of the reconstructed data with the convolution of the GEANT4 simulation of the scattering in the absorber convolved with the empty absorber data at 172 MeV/c, 200 MeV/c and 240 MeV/c are shown in Fig. 11.

4.2 Deconvolution

To determine the RMS scattering angle from the underlying scattering distribution, the effects of scattering in non-absorber materials and the detector resolution must be deconvolved from the measured scattering distribution. The measured scattering distribution with the absorber in the MICE channel can be stated as:

$$x'(i) = \sum_{k=0}^{i} x(k)h(i-k) + n(i) = x(i) * h(i) + n(i), \tag{9}$$

where $x'(i)$ is the distribution measured with the absorber in the channel, $x(k)$ is the scattering distribution due only to the absorber material without the detector, $h(i-k)$ is the scattering distribution of the empty absorber with the detector and $n(i)$ an additive noise. This system of linear equations can be written in matrix form as:

$$x' = Hx + n \tag{10}$$

The variable $||Hx - x'||^2$ is minimised to find an optimal solution. The unfolding step employs Gold's deconvolution algorithm, to extract the true scattering due to the absorber material, as described in [29] and implemented in the ROOT class TSpectrum. This method has the advantage over other methods in that it does not rely on simulated data or scattering models and is a purely data-driven technique making use of all of the data collected.

The method iterates over the data points $x_i^{(k)}$ in bin i and iteration k,

$$x_i^{(k+1)} = \frac{x_i'}{\sum_{m=0}^{N-1} H_{im}' x_m^{(k)}} x_i^{(k)}, \tag{11}$$

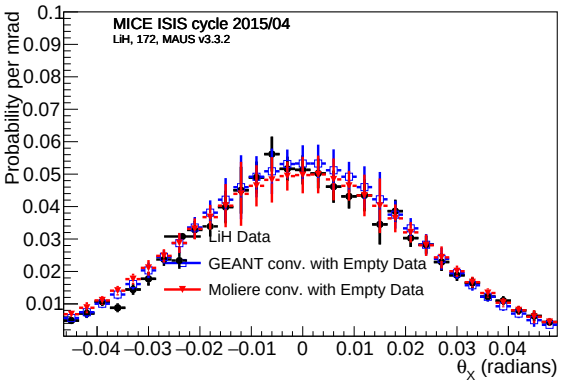

(a) θ_x scattering distribution at 172 MeV/c.

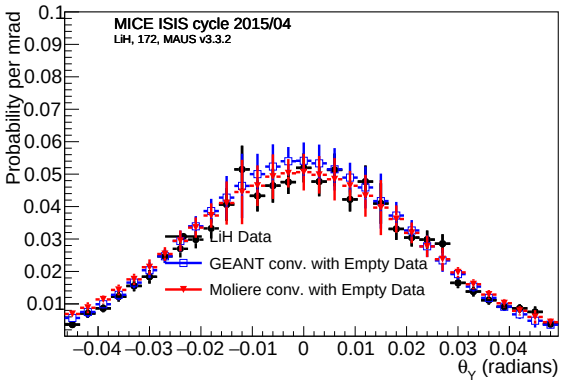

(b) θ_y scattering distribution at 172 MeV/c.

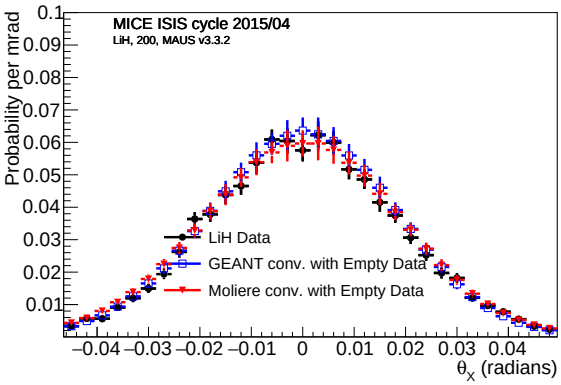

(c) θ_x scattering distribution at 200 MeV/c.

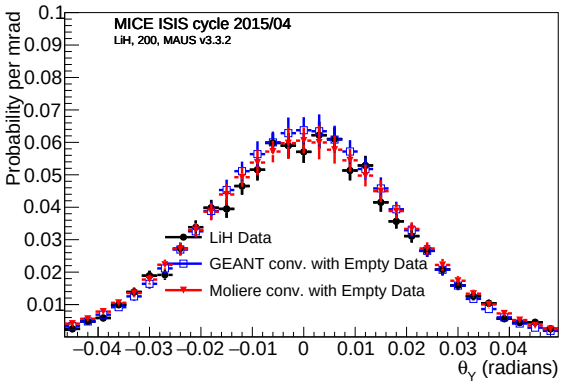

(d) θ_y scattering distribution at 200 MeV/c.

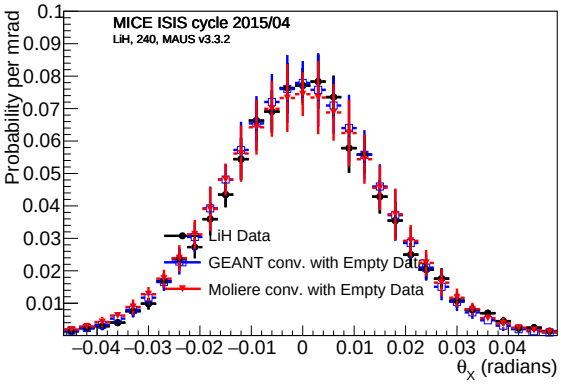

(e) θ_x scattering distribution at 240 MeV/c.

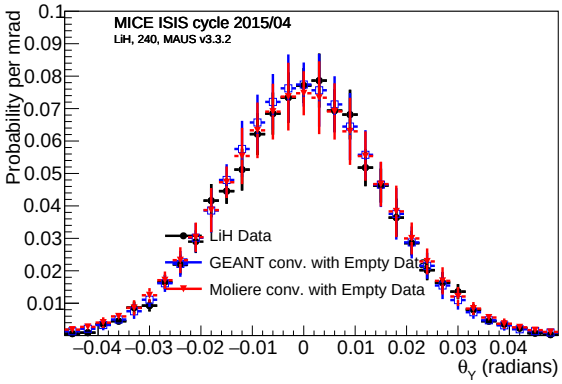

(f) θ_y scattering distribution at 240 MeV/c.

Figure 11: Scattering distributions reconstructed from the 172 MeV/c, 200 MeV/c and 240 MeV/c muon beams with the LiH absorber in place (black dots) compared to the GEANT4 scattering model (blue dots) and the Molière model (red dots) in LiH convolved with the scattering data taken without the LiH absorber in place.

with

$$\begin{aligned} i &= 0, 1, ..., N-1, \\ k &= 1, 2, 3, ..., L, \\ x^{(0)} &= [1, 1, ..., 1]^T, \end{aligned} \tag{12}$$

where H'_{im} is a Toeplitz matrix, with N the number of bins and where L is the total number of iterations. The algorithm typically converged to a solution after ~ 10 iterations.

4.3 Systematic uncertainties

Six different contributions to the systematic uncertainty in the scattering distributions are considered here: uncertainties in the time of flight due to the resolution and momentum estimation, uncertainties in the measured alignment, uncertainties in the fiducial radius, the scattering angle definition, the effect of pion contamination and the deconvolution procedure. The uncertainty in the measured width of the distribution is calculated using a standardised formulation

$$\sigma_{sys} \approx \frac{\sigma_\alpha}{\Delta\alpha}\Delta\theta_0, \tag{13}$$

where $\Delta\theta_0$ is the change in the distribution width that results from altering a parameter α with a known error σ_α in the analysis or simulation by a quantity $\Delta\alpha$. Each of the systematic uncertainties is defined from the difference obtained by varying by the uncertainty in the parameter divided by the change in parameter. The systematic uncertainties are added on a bin by bin basis to the uncertainties used in the calculation of the χ^2 shown in Equation 8 using the same scaling factor. The systematic uncertainties are reported for the RMS width of the θ_x distribution ($\theta_{0,x}$) and the width of the θ_y distribution ($\theta_{0,y}$) separately.

A significant systematic uncertainty is due to the TOF selection criteria, which directly impacts the momentum range of the particles used in the scattering measurement. The scale is set by the 70 ps resolution of the time-of-flight measurements. The effect of particles incorrectly appearing inside or outside of the 200 ps selection window is determined by offsetting the empty channel data by 200 ps and the difference in the measured scattering width, scaled by a factor of $\sigma_\alpha/\Delta\alpha = 70\ \mathrm{ps}/200\ \mathrm{ps}$, is treated as the systematic uncertainty.

Uncertainties in the alignment have a direct effect on the angles measured by the tracker. The alignment of the MICE trackers is characterized by four parameters defining offsets, with an uncertainty of 0.2 mm, and angles, with an uncertainty of 0.07 mrad in the X-Z and Y-Z planes. The z position of the tracker and rotations about the z axis are not accessible to the alignment. The alignment of the upstream and downstream trackers are independent, so there is a total number of eight alignment parameters. A number of pseudo-experiments were simulated by varying the values of all of the alignment parameters within their uncertainties. The uncertainties in the width of the scattering distributions is extracted from the ensemble of the measurements from the pseudo-experiments.

The choice of the fiducial region may systematically affect the results. A scan over the possible values of the fiducial radius and gradient was completed and the difference between the scattering width of the grid points adjacent to the selection values of 90 mm and 12 mrad are used to set the uncertainty with a scaling factor based on the uncertainties in position and angle which are 0.495 mm and 0.56 mrad respectively. The differences measured from changes in the fiducial gradient are then scaled by 0.56 mrad/10 mrad = 0.056, and the differences measured from changes in the fiducial radius are scaled by 0.495 mm/20 mm = 0.0248 to get the systematic uncertainties for the fiducial selection. The scattering width is insensitive to the radial fiducial selection, with systematic uncertainties at the sub-percent level. In contrast, the gradient used in the fiducial selection has a larger effect, approaching 1% for the deconvolved results. These are included in Table 4.

The definitions of the scattering angles is given in section 2 and the Appendix. Equations 17 and 18 give the definition of the projected scattering angles, where

$$\hat{\mathbf{v}} = \mathbf{s} \times \hat{\mathbf{u}}, \tag{14}$$

and $\mathbf{s}$ is arbitrarily defined as $\mathbf{s} = (0, -1, 0)$. This expression defines the plane which contains the upstream track. There is an infinite number of planes that contain this track, so we consider the uncertainty introduced by the definition of $\mathbf{s}$ by rotating it between 0° and 180° around the x-axis, with the analysis repeated at each point. The resulting maximum change in measured scattering angle is included into the systematic uncertainties Table 4.

The MICE muon beam has pion contamination with an upper limit of $f_\pi < 1.4\%$ at 90% C.L. [24]. To measure the effect of this contamination on the scattering measurement for muons, a Monte Carlo study was performed. The measurement was made with a simulation of the real MICE muon beam and a pure muon sample, with the systematic error being the difference between the two results.

The difference between the deconvolved result and the true scattering distribution from a GEANT4 simulation was taken to be an additional source of systematic error. This accounts for any bias introduced by the Gold deconvolution procedure. The systematic uncertainties for the deconvolution procedure showed significant variation from bin to bin so a parabolic smoothing function was used to assign the systematic uncertainty to each bin.

All systematic uncertainties for the three selected momenta of 172 MeV/c, 200 MeV/c and 240 MeV/c and their quadratic combination are included in Table 4. The dominant systematic uncertainties are due to the momentum measurement due to the TOF and due to the deconvolution procedure.

4.4 Results

The deconvolved θ_x and θ_y multiple scattering distributions on lithium hydride, taken with the 172 MeV/c, 200 MeV/c and 240 MeV/c muon samples are shown in Fig. 12, and these are compared against a GEANT4 LiH simulation and the Molière calculation. There is very little difference between the GEANT4 simulation, the Molière calculations and the deconvolved data.

The residuals between the data, the full GEANT4 simulation and the raw Geant4 simulation convolved with the Empty absorber data appear in Fig. 13. The χ^2 derived from these residuals appear in Table 5. The χ^2 was calculated assuming 29 data points and show good agreement with data.

The fluctuations dominate the processed distribution at angles greater than 45 mrad for the data and simulation, signifying that angular acceptance of the channel is low in these regions and that a statement about scattering cannot reasonably be made as expected from Fig. 3. The distributions of the projections in θ_x and θ_y were characterized using a Gaussian fit within a ± 45 mrad range, with the results shown in Table 6 for deconvolved data using the Gold deconvolution algorithm and the true distributions extracted from the raw GEANT4 simulation and the Molière model calculation. The table shows that the deconvolved θ_x and θ_y projections of the scattering distributions are roughly consistent with the GEANT4 and Molière distributions, but the Molière distribution is systematically wider than the rest. The χ^2/NDF values of the distribution are assumed to be uncorrelated.

4.5 Momentum-dependent measurements

The muon beam data can be sub-divided to measure the momentum dependence of the multiple scattering distributions. A procedure was used to select time-of-flight bins, which may be plotted as a function of mean

Table 4: Systematic uncertainties associated to the width of the scattering distributions of $\theta_{0,x}$ and $\theta_{0,y}$ as a function of momentum after deconvolution.

$\langle p \rangle$ (MeV/c)	Type	$\Delta\theta_{0,x}$ (mrad)	$\Delta\theta_{0,y}$ (mrad)
170.48±0.07	TOF	0.67	0.67
	Alignment	0.00	0.01
	Fiducial radius	0.01	0.01
	Scattering angle definition	0.00	0.00
	Pion contamination	0.00	0.01
	Deconvolution	1.16	0.64
	Total sys.	1.34	0.93
196.97±0.06	TOF	0.34	0.34
	Alignment	0.00	0.00
	Fiducial radius	0.01	0.02
	Scattering angle definition	0.00	0.00
	Pion contamination	0.01	0.01
	Deconvolution	0.41	0.48
	Total sys.	0.53	0.59
234.57±0.08	TOF	0.30	0.30
	Alignment	0.00	0.00
	Fiducial radius	0.00	0.00
	Scattering angle definition	0.00	0.00
	Pion contamination	0.00	0.00
	Deconvolution	0.28	0.43
	Total sys.	0.41	0.52

Table 5: Measurements of distribution widths of multiple scattering in lithium hydride and the χ^2 comparisons between data, the full GEANT4 simulation, the raw GEANT4 simulation convolved with empty absorber data and the Molière scattering model convolved with empty absorber data. The χ^2/NDF were calculated using number of bins as number of degrees of freedom. Statistical and systematic uncertainties have been given for the data distributions. Only statistical uncertainties are given for the models.

p	Angle	Θ_{Data} (mrad)	Θ_{G4} (mrad)	χ^2/NDF	$\Theta_{G4\otimes Empty}$ (mrad)	χ^2/NDF	$\Theta_{Mol\otimes Empty}$ (mrad)	χ^2/NDF
170.48	θ_x	21.19±0.28±0.49	22.09±0.27	21.95 / 29	21.38±0.07	22.43 / 29	22.56±0.09	28.46 / 29
170.48	θ_y	21.22±0.28±0.49	21.95±0.27	28.94 / 29	21.13±0.07	23.86 / 29	22.39±0.08	28.17 / 29
196.97	θ_x	18.59±0.19±0.36	19.17±0.09	18.54 / 29	18.33±0.03	26.38 / 29	19.21±0.03	34.70 / 29
196.97	θ_y	18.62±0.18±0.36	19.15±0.09	26.32 / 29	18.19±0.03	29.19 / 29	19.12±0.03	28.00 / 29
234.57	θ_x	15.39±0.16±0.20	16.07±0.06	13.32 / 29	15.18±0.02	12.24 / 29	15.71±0.02	17.75 / 29
234.57	θ_y	15.23±0.14±0.20	15.98±0.06	28.05 / 29	15.14±0.02	12.54 / 29	15.74±0.02	25.88 / 29

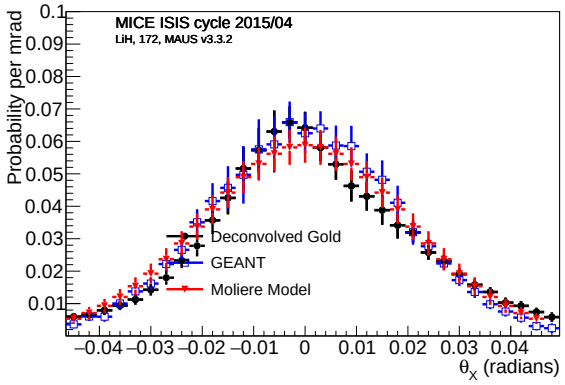

(a) θ_x scattering distribution at 172 MeV/c.

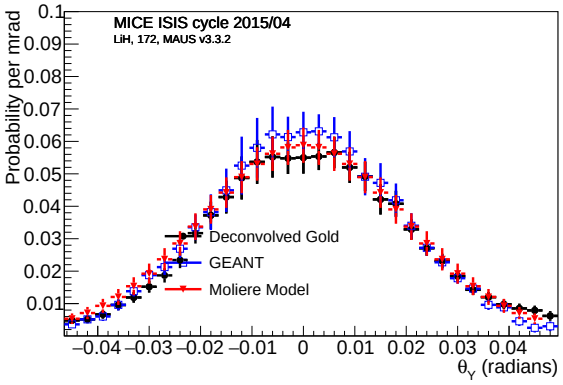

(b) θ_y scattering distribution at 172 MeV/c.

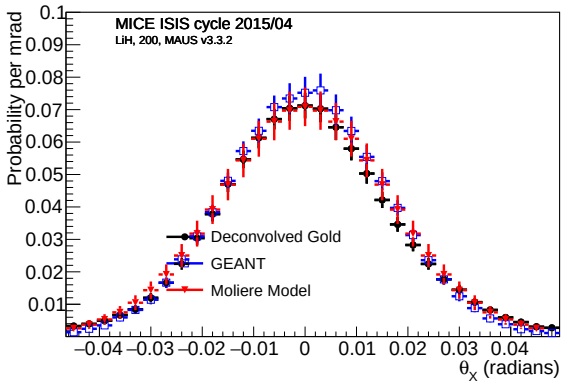

(c) θ_x scattering distribution at 200 MeV/c.

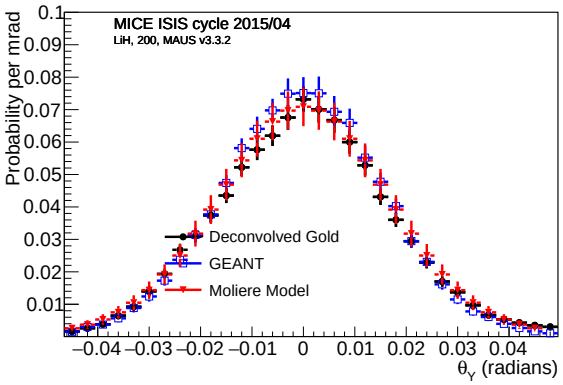

(d) θ_y scattering distribution at 200 MeV/c.

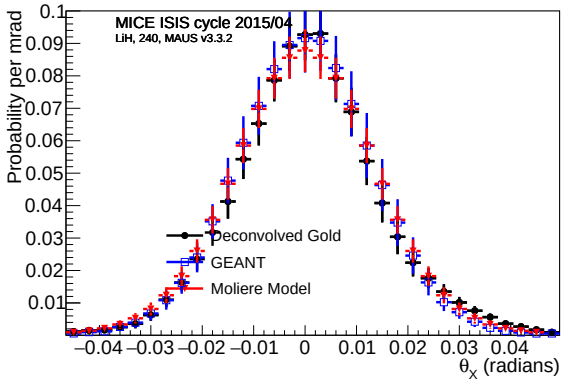

(e) θ_x scattering distribution at 240 MeV/c.

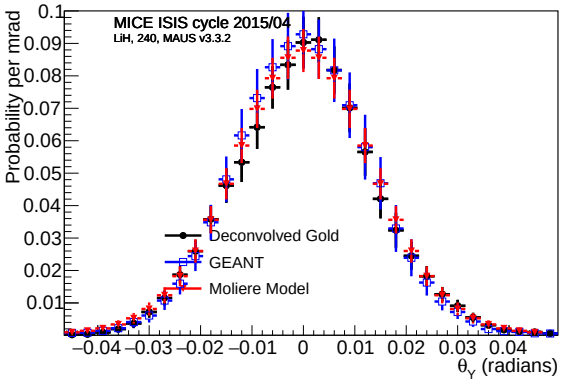

(f) θ_y scattering distribution at 240 MeV/c.

Figure 12: Projected θ_x and θ_y multiple scattering distributions at 172 MeV/c, 200 MeV/c and 240 MeV/c after deconvolution. The GEANT4 and Molière scattering distributions in LiH are provided for comparison.

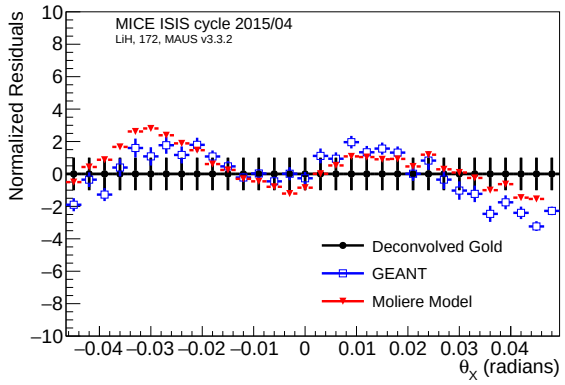

(a) Residuals from θ_x scattering distribution at 172 MeV/c.

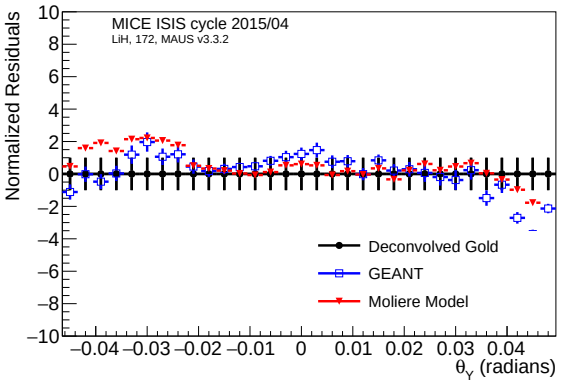

(b) Residuals from θ_y scattering distribution at 172 MeV/c.

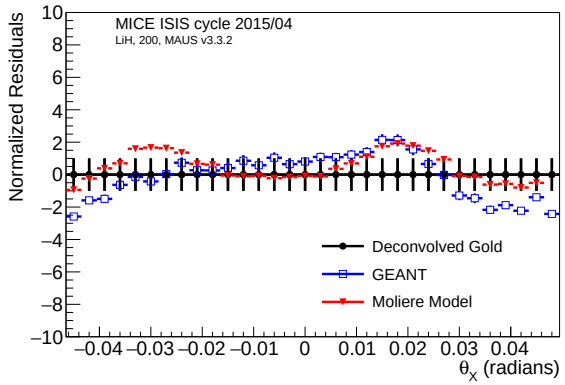

(c) Residuals from θ_x scattering distribution at 200 MeV/c.

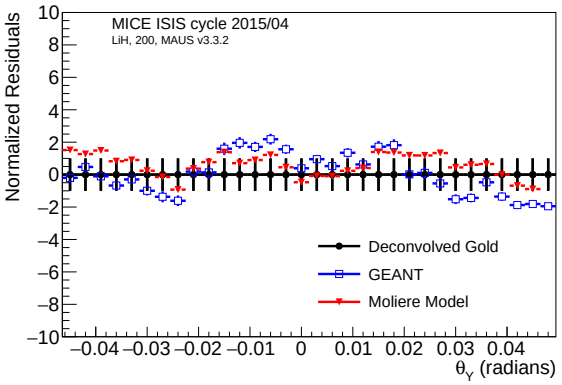

(d) Residuals from θ_y scattering distribution at 200 MeV/c.

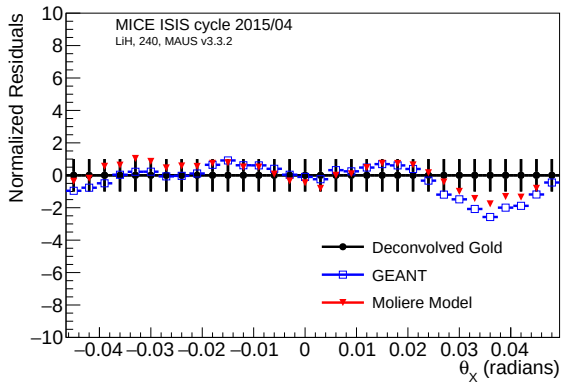

(e) Residuals from θ_x scattering distribution at 240 MeV/c.

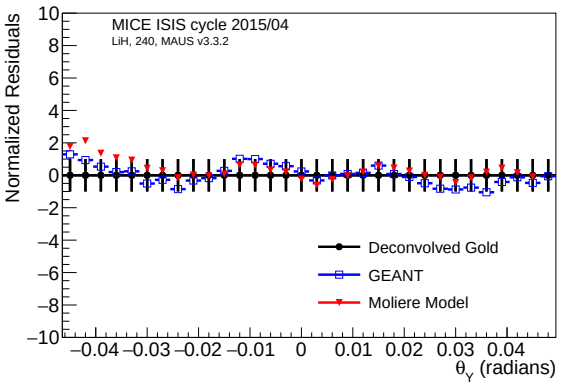

(f) Residuals from θ_y scattering distribution at 240 MeV/c.

Figure 13: Scattering residuals between deconvolved data from a muon beam with the LiH absorber in place compared to the GEANT4 and Molière scattering models in LiH.

Table 6: Measurements of distribution widths and χ^2/NDF comparison between the data after deconvolution of spectra and two different models (GEANT4 and Molière). The χ^2/NDF of the distributions are assumed to be uncorrelated. Statistical and systematic uncertainties have been given for the data distributions. Only statistical uncertainties are given for the models.

p	Angle	Θ^{meas}_{Gold} (mrad)	Θ^{true}_{G4} (mrad)	χ^2/NDF	$\Theta^{true}_{Moliere}$ (mrad)	χ^2/NDF
170.48	θ_x	19.46±0.28±1.34	18.62±0.13	25.13 / 29	20.26±0.00	30.74 / 29
170.48	θ_y	19.70±0.26±0.93	18.59±0.12	12.46 / 29	20.26±0.00	27.29 / 29
196.97	θ_x	16.61±0.18±0.53	15.82±0.05	72.41 / 29	16.97±0.00	43.65 / 29
196.97	θ_y	16.64±0.17±0.59	15.82±0.05	59.68 / 29	16.97±0.00	34.69 / 29
234.57	θ_x	13.41±0.17±0.41	13.16±0.04	17.40 / 29	13.85±0.00	11.99 / 29
234.57	θ_y	13.45±0.15±0.52	13.10±0.04	7.41 / 29	13.85±0.00	36.61 / 29

momentum in each bin, to confirm the momentum-dependence of the widths of the scattering distributions. The number of events contained in each TOF bin is between 3000 and 9000 events. The deconvolved scattering widths as a function of momentum are shown in Fig. 14 and the results are fit to the function

$$\theta_0 = \frac{13.6\,[\mathrm{MeV/c}]a}{p\beta}, \tag{15}$$

where a is a fit coefficient, motivated by Equation 3. The coefficient of the momentum-dependent term is compared with the prediction from the PDG formula $a = \sqrt{\frac{z}{X_0}}\left(1 + 0.0038 \ln \frac{z}{X_0}\right)$.

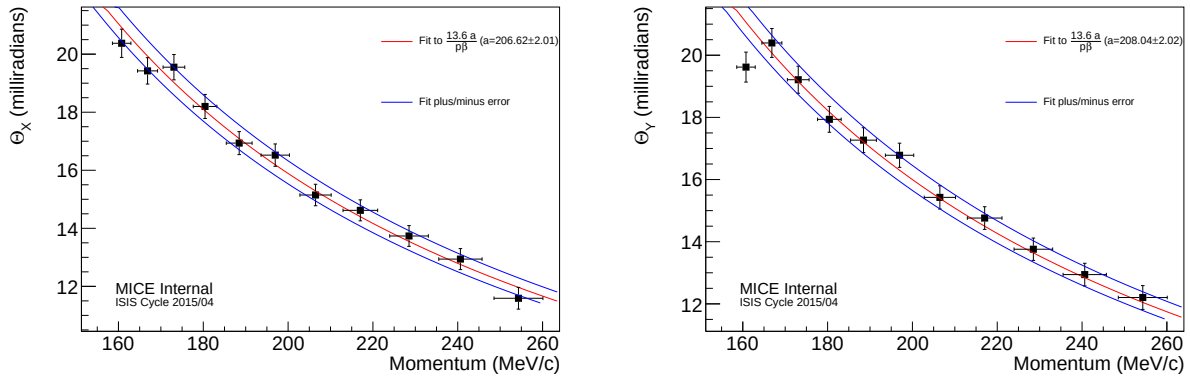

(a) Width in scattering angle $\theta_{0,x}$.

(b) Width in scattering angle $\theta_{0,y}$.

Figure 14: The results of the scattering analysis using data from all three nominal beam settings. Scattering widths are reported after application of the Gold deconvolution, using the GEANT4 model.

The parameters resulting from these fits are shown in Fig. 14. The values of the coefficients a determined from the fits to the $\theta_{0,x}$ and $\theta_{0,y}$ distributions are shown in Table 7. The systematic uncertainty associated with the momentum scale was assessed by using the results of an empirical fit between the reconstructed corrected momentum and time of flight $t_\mu = m/p_\mu + c$, shown in Fig. 4, with m = 860.95±31 ns·MeV/c and $c = 23.68 \pm 0.20$ ns. The statistical uncertainties are determined by the estimate of the derivative of θ with respect to momentum multiplied by the variation of the momentum with respect to the time-of-flight, multiplied

by the time-of-flight uncertainty

$$\sigma_\theta = \frac{d\theta}{dp}\frac{dp}{dt_{TOF}}\sigma_{TOF} = \frac{\theta(p + 4\text{ MeV/c}) - \theta(p - 4\text{ MeV/c})}{8\text{ MeV/c}}\frac{m}{(t_{TOF} - c)^2}\sigma_{TOF}, \tag{16}$$

with $\sigma_{TOF} = 70$ ns as defined for the time-of-flight systematic uncertainty. The limits of the fitted uncertainty, given by the blue lines in Fig. 14, include the systematic uncertainties.

Measurements using the projected angles are systematically smaller than the PDG prediction, as shown in Fig. 14 and in Table 7. The average of the two fits to the $\theta_{0,x}$ and $\theta_{0,y}$ muon scattering widths as a function of momentum yields $a = 207.3 \pm 1.4$ mrad, which is 9% smaller than the value proposed by the PDG formula, $a = 226.7$ mrad, but still within the uncertainties of that approximate formula.

Table 7: Results of the fit to the scattering widths as a function of momentum, given by Equation 15. The value consistent with the PDG prediction is also shown.

Angle	a (mrad)
$\theta_{0,x}$	206.6±2.0
$\theta_{0,y}$	208.0±2.0
PDG	226.7

5 Conclusions

Presented here is an analysis of the lithium hydride (LiH) multiple Coulomb scattering data compiled over ISIS user run 2015/04 using the Muon Ionization Cooling Experiment (MICE). These data were compared to different implementations of multiple scattering in LiH, including the compact implementation used as the GEANT4 (v9.6) default [11] and the full Molière calculation [3, 4]. A χ^2 statistic was used to make qualitative statements about the validity of the proposed models. The GEANT4 scattering widths agree with the measured data at each of the central momenta, but the Molière model produces systematically wider distributions. A deconvolution procedure was then applied to the data with the same conclusion. Widths from the scattering distributions projected onto the X-Z and Y-Z planes produce consistent results between the data and GEANT4, but the Molière model shows scattering widths that are systematically larger. The scattering measurements yield $\theta_0 = 19.58 \pm 0.27 \pm 1.14$ mrad at 170.5 MeV/c, $\theta_0 = 16.63 \pm 0.18 \pm 0.56$ mrad at 197.0 MeV/c, and $\theta_0 = 13.43 \pm 0.16 \pm 0.47$ mrad at 234.6 MeV/c in LiH. These results are consistent with the GEANT4 and Molière predictions.

The momentum dependence of scattering was examined by considering 200 ps time-of-flight selections from the muon beam data. This momentum dependence from 160 MeV/c to 255 MeV/c was compared to the dependence in Equation 3 from the PDG [9] and it was found that the measured RMS scattering width is about 9% smaller than the approximate PDG estimation, but within its stated uncertainty.

Appendix

The projection of the scattering angle onto the Y-Z or X-Z plane, angles θ_x and θ_y, are defined by considering the inner product of the downstream momentum $\mathbf{p}_{DS}$ with the component of the upstream momentum vector $\mathbf{p}_{US}$, perpendicular to the projection plane. The scattering projection into the plane defined by the momentum

vector and the y-axis is

$$\theta_y = \arctan\left(\frac{\mathbf{p}_{DS}\cdot\hat{\mathbf{u}}}{\mathbf{p}_{DS}\cdot\hat{\mathbf{v}}}\right) = \arctan\left(\frac{\mathbf{p}_{DS}\cdot(\hat{\mathbf{y}}\times\mathbf{p}_{US})|\mathbf{p}_{US}|}{(\mathbf{p}_{DS}\cdot\mathbf{p}_{US})|\hat{\mathbf{y}}\times\mathbf{p}_{US}|}\right), \tag{17}$$

where $\hat{\mathbf{y}}$ is the unit vector in the y direction, $\hat{\mathbf{v}} = \hat{\mathbf{y}}\times\mathbf{p}_{US}/|\hat{\mathbf{y}}\times\mathbf{p}_{US}|$ is the unit vector mutually orthogonal to the y direction and the momentum vector and $\hat{\mathbf{u}} = \mathbf{p}_{US}/|\mathbf{p}_{US}|$ is the unit vector parallel to the upstream momentum vector. A scattering angle in the perpendicular plane must then be defined as

$$\theta_x = \arctan\left(|\mathbf{p}_{US}|\frac{\mathbf{p}_{DS}\cdot(\mathbf{p}_{US}\times(\hat{\mathbf{y}}\times\mathbf{p}_{US}))}{|\mathbf{p}_{US}\times(\hat{\mathbf{y}}\times\mathbf{p}_{US})|\mathbf{p}_{DS}\cdot\mathbf{p}_{US}}\right), \tag{18}$$

where the downstream vector is now projected onto the unit vector $\hat{\mathbf{v}} = \mathbf{p}_{US}\times(\hat{\mathbf{y}}\times\mathbf{p}_{US})/|\mathbf{p}_{US}\times(\hat{\mathbf{y}}\times\mathbf{p}_{US})|$. These two expressions can be expressed in terms of the gradients of the muon tracks before and after the scatters,

$$\theta_y = \arctan\left(\frac{\sqrt{1+\left(\frac{dx}{dz}\right)^2_{US}+\left(\frac{dy}{dz}\right)^2_{US}}}{\sqrt{1+\left(\frac{dx}{dz}\right)^2_{US}}}\left\{\frac{\left(\frac{dx}{dz}\right)_{DS}-\left(\frac{dx}{dz}\right)_{US}}{1+\left(\frac{dx}{dz}\right)_{US}\left(\frac{dx}{dz}\right)_{DS}+\left(\frac{dy}{dz}\right)_{US}\left(\frac{dy}{dz}\right)_{DS}}\right\}\right), \tag{19}$$

$$\theta_x = \arctan\left(\sqrt{\frac{1+\left(\frac{dx}{dz}\right)^2_{US}+\left(\frac{dy}{dz}\right)^2_{US}}{\left(1+\left(\frac{dx}{dz}\right)^2_{US}+\left(\frac{dy}{dz}\right)^2_{US}\right)\left(1+\left(\frac{dx}{dz}\right)^2_{US}\right)}}\right.$$

$$\left.\times\left\{\frac{\left(\frac{dy}{dz}\right)_{DS}\left(1+\left(\frac{dx}{dz}\right)^2_{US}\right)+\left(\left(\frac{dx}{dz}\right)_{DS}\left(\frac{dx}{dz}\right)_{US}-1\right)\left(\frac{dy}{dz}\right)_{US}}{1+\left(\frac{dx}{dz}\right)_{US}\left(\frac{dx}{dz}\right)_{DS}+\left(\frac{dy}{dz}\right)_{US}\left(\frac{dy}{dz}\right)_{DS}}\right\}\right). \tag{20}$$

In the approximation of small angles (i.e. $\frac{dx}{dz}\approx\frac{dy}{dz}\ll 1$) these produce the more familiar forms

$$\theta_x = \left(\frac{dy}{dz}\right)_{DS} - \left(\frac{dy}{dz}\right)_{US} \tag{21}$$

for scattering about the x-axis or

$$\theta_y = \left(\frac{dx}{dz}\right)_{DS} - \left(\frac{dx}{dz}\right)_{US} \tag{22}$$

for scattering about the y-axis. The more exact expressions, equations 19 and 20, are used throughout for this analysis.

References

[1] B. Rossi and K. Greisen, "Cosmic-ray theory," *Rev. Mod. Phys.* **13** (1941) 240–309.

[2] E. Rutherford, "The scattering of alpha and beta particles by matter and the structure of the atom," *Phil. Mag. Ser.6* **21** (1911) 669–688.

[3] G. Molière, "Theorie der Streuung schneller geladener Teilchen I. Einzelstreuung am abgeschirmten Coulomb-Feld," *Z. Naturforsch.* **A2** (1947) 133.

[4] G. Molière, "Theory of the scattering of fast charged particles. 2. Repeated and multiple scattering," *Z. Naturforsch.* **A3** (1948) 78–97.

[5] H. A. Bethe, "Moliere's theory of multiple scattering," *Phys. Rev.* **89** (1953) 1256–1266.

[6] U. Fano, "Inelastic Collisions and the Moliere Theory of Multiple Scattering," *Phys. Rev.* **93** (1954) 117–120.

[7] V. L. Highland, "Some Practical Remarks on Multiple Scattering," *Nucl. Instrum. Meth.* **129** (1975) 497.

[8] G. R. Lynch and O. I. Dahl, "Approximations to multiple Coulomb scattering," *Nucl. Instrum. Meth.* **B58** (1991) 6–10.

[9] **Particle Data Group** Collaboration, P. Zyla *et al.*, "Review of Particle Physics," *PTEP* **2020** no. 8, (2020) 083C01. p. 535-550.

[10] D. Attwood *et al.*, "The scattering of muons in low Z materials," *Nucl. Instrum. Meth.* **B251** (2006) 41–55, arXiv:hep-ex/0512005 [hep-ex].

[11] **GEANT4** Collaboration, S. Agostinelli *et al.*, "GEANT4: A Simulation toolkit," *Nucl. Instrum. Meth.* **A506** (2003) 250–303.

[12] G. Wentzel, "Zwei Bemerkungen über die Zerstreuung korpuskularer Strahlen als Beugungserscheinung," *Z. Phys.* **40** no. 8, (1926) 590–593.

[13] T. Carlisle, *Step IV of the Muon Ionization Cooling Experiment (MICE) and the multiple scattering of muons*. PhD thesis, Oxford U., 2013. http://mice.iit.edu/phd/TimCarlisle-thesis.pdf.

[14] G. Gregoire *et al.*, "Proposal to the Rutherford Appleton Laboratory: an international muon ionization cooling experiment (MICE)," in *MICE Collaboration Meeting CM4 Berkeley, USA, October 23-26, 2002*. 2003. http://mice.iit.edu/mnp/MICE0021.pdf.

[15] **MICE** Collaboration, M. Bogomilov *et al.*, "Demonstration of cooling by the Muon Ionization Cooling Experiment," *Nature* **578** no. 7793, (2020) 53–59, arXiv:1907.08562 [physics.acc-ph].

[16] M. Bogomilov *et al.*, "Neutrino Factory," *Phys. Rev. ST Accel. Beams* **17** no. 12, (2014) 121002.

[17] D. Neuffer, P. Snopok, and Y. Alexahin, "Front End for a Neutrino Factory or Muon Collider," *JINST* **12** no. 11, (2017) T11007, arXiv:1711.11120 [physics.acc-ph].

[18] **MICE** Collaboration, M. Bogomilov *et al.*, "The MICE Muon Beam on ISIS and the beam-line instrumentation of the Muon Ionization Cooling Experiment," *JINST* **7** (2012) P05009, arXiv:1203.4089 [physics.acc-ph].

[19] **MICE** Collaboration, D. Adams *et al.*, "Characterisation of the muon beams for the Muon Ionisation Cooling Experiment," *Eur. Phys. J.* **C73** no. 10, (2013) 2582, arXiv:1306.1509 [physics.acc-ph].

[20] M. Ellis *et al.*, "The Design, construction and performance of the MICE scintillating fibre trackers," *Nucl. Instrum. Meth.* **A659** (2011) 136–153, arXiv:1005.3491 [physics.ins-det].

[21] C. N. Booth *et al.*, "The design, construction and performance of the MICE target," *JINST* **8** (2013) P03006, arXiv:1211.6343 [physics.ins-det].

[22] C. N. Booth *et al.*, "The design and performance of an improved target for MICE," *JINST* **11** no. 05, (2016) P05006, arXiv:1603.07143 [physics.ins-det].

[23] **MICE** Collaboration, R. Bertoni *et al.*, "The design and commissioning of the MICE upstream time-of-flight system," *Nucl. Instrum. Meth.* **A615** (2010) 14–26, arXiv:1001.4426 [physics.ins-det].

[24] **MICE** Collaboration, M. Bogomilov *et al.*, "Pion Contamination in the MICE Muon Beam," *JINST* **11** no. 03, (2016) P03001, arXiv:1511.00556 [physics.ins-det].

[25] **MICE** Collaboration, D. Adams *et al.*, "Electron-Muon Ranger: performance in the MICE Muon Beam," *JINST* **10** no. 12, (2015) P12012, arXiv:1510.08306 [physics.ins-det].

[26] C. D. Tunnell and C. T. Rogers, "MAUS: MICE Analysis User Software," *Conf. Proc.* **C110904** (2011) 850–852.

[27] R. Asfandiyarov *et al.*, "MAUS: the MICE analysis user software," *JINST* **14** no. 04, (2019) T04005, arXiv:1812.02674 [physics.comp-ph].

[28] A. Dobbs, C. Hunt, K. Long, E. Santos, M. A. Uchida, P. Kyberd, C. Heidt, S. Blot, and E. Overton, "The reconstruction software for the MICE scintillating fibre trackers," *JINST* **11** no. 12, (2016) T12001, arXiv:1610.05161 [physics.ins-det].

[29] M. Morhac, J. Kliman, V. Matousek, M. Veselsky, and I. Turzo, "Efficient one- and two-dimensional Gold deconvolution and its application to γ-ray spectra decomposition," *Nucl. Instr. and Meth. A* **401** no. 2-3, (1997) 385–408.

Author List

M. Bogomilov, R. Tsenov, G.Vankova-Kirilova
Department of Atomic Physics, St. Kliment Ohridski University of Sofia, Sofia, Bulgaria

Y. Song, J. Tang
Institute of High Energy Physics, Chinese Academy of Sciences, Beijing, China

Z. Li
Sichuan University, China

R. Bertoni, M. Bonesini, F. Chignoli, R. Mazza
Sezione INFN Milano Bicocca, Dipartimento di Fisica G. Occhialini, Milano, Italy

V. Palladino
Sezione INFN Napoli and Dipartimento di Fisica, Università Federico II,Complesso Universitario di Monte S. Angelo, Napoli, Italy

A. de Bari, G. Cecchet
Sezione INFN Pavia and Dipartimento di Fisica Nucleare e Teorica, Pavia, Italy

D. Orestano, L. Tortora
INFN Sezione di Roma Tre and Dipartimento di Matematica e Fisica, Universit'a Roma Tre, Italy

Y. Kuno
Osaka University, Graduate School of Science, Department of Physics, Toyonaka, Osaka, Japan

S. Ishimoto
High Energy Accelerator Research Organization (KEK), Institute of Particle and Nuclear Studies, Tsukuba, Ibaraki, Japan

F. Filthaut
Nikhef, Amsterdam, The Netherlands and Radboud University, Nijmegen, The Netherlands

D. Jokovic, D. Maletic, M. Savic
Institute of Physics, University of Belgrade, Serbia

O. M. Hansen,, S. Ramberger, M. Vretenar
CERN, Geneva, Switzerland

R. Asfandiyarov, A. Blondel, F. Drielsma,, Y. Karadzhov
DPNC, Section de Physique, Université de Genève, Geneva, Switzerland

G. Charnley, N. Collomb, K. Dumbell, A. Gallagher, A. Grant, S. Griffiths, T. Hartnett, B. Martlew, A. Moss, A. Muir, I. Mullacrane, A. Oates, P. Owens, G. Stokes, P. Warburton, C. White
STFC Daresbury Laboratory, Daresbury, Cheshire, UK

D. Adams, R.J. Anderson, P. Barclay, V. Bayliss, J. Boehm,, T. W. Bradshaw, M. Courthold, V. Francis, L. Fry, T. Hayler, M. Hills, A. Lintern, C. Macwaters, A. Nichols, R. Preece, S. Ricciardi, C. Rogers, T. Stanley, J. Tarrant, M. Tucjker, A. Wilson
STFC Rutherford Appleton Laboratory, Harwell Oxford, Didcot, UK

S. Watson
STFC Rutherford UK Astronomy Technology Centre, Royal Observatory, Edinburgh, Blackford Hill, Edinburgh EH9 3HJ, UK

R. Bayes, J. C. Nugent, F. J. P. Soler
School of Physics and Astronomy, Kelvin Building, The University of Glasgow, Glasgow, UK

R. Gamet
Department of Physics, University of Liverpool, Liverpool, UK

G. Barber, V. J. Blackmore, D. Colling, A. Dobbs, P. Dornan, C. Hunt, A. Kurup, J-B. Lagrange, K. Long, J. Martyniak, S. Middleton, J. Pasternak, M. A. Uchida
Department of Physics, Blackett Laboratory, Imperial College London, London, UK

J. H. Cobb, W. Lau
Department of Physics, University of Oxford, Denys Wilkinson Building, Oxford, UK

C. N. Booth, P. Hodgson, J. Langlands, E. Overton, M. Robinson, P. J. Smith, S. Wilbur
Department of Physics and Astronomy, University of Sheffield, Sheffield, UK

A. Dick, K. Ronald, C. G. Whyte, A. R. Young
SUPA and the Department of Physics, University of Strathclyde, Glasgow, UK and Cockroft Institute, UK

S. Boyd, P. Franchini, J. R. Greis, C. Pidcott, I. Taylor
Department of Physics, University of Warwick, Coventry, UK

R. B. S. Gardener, P. Kyberd, J. J. Nebrensky
Brunel University, Uxbridge, UK

M. Palmer, H. Witte
Brookhaven National Laboratory, NY, USA

A. D. Bross, D. Bowring, A. Liu, D. Neuffer, M. Popovic, P. Rubinov
Fermilab, Batavia, IL, USA

A. DeMello, S. Gourlay, D. Li, S. Prestemon, S. Virostek
Lawrence Berkeley National Laboratory, Berkeley, CA, USA

B. Freemire, P. Hanlet, D. M. Kaplan, D. Rajaram, P. Snopok, V. Suezaki, Y. Torun
Illinois Institute of Technology, Chicago, IL, USA

Y. Onel
Department of Physics and Astronomy, University of Iowa, Iowa City, IA, USA

L. M. Cremaldi, D. A. Sanders, D. J. Summers
University of Mississippi, Oxford, MS, USA

G. G. Hanson, C. Heidt
University of California, Riverside, CA, USA